UC San Diego
UC San Diego Previously Published Works

Title

Chromosome segregation errors generate a diverse spectrum of simple and complex genomic rearrangements

Permalink

Journal

ISSN

Authors

Ly, Peter
Brunner, Simon F
Shoshani, Ofer
et al.

Publication Date

DOI

Peer reviewed

Chromosome Segregation Errors Generate a Diverse Spectrum of Simple and Complex Genomic Rearrangements

Peter Ly[1,9], **Simon F. Brunner**[2], **Ofer Shoshani**[1], **Dong Hyun Kim**[1], **Weijie Lan**[1], **Tatyana Pyntikova**[3], **Adrienne M. Flanagan**[4,5], **Sam Behjati**[2,6], **David C. Page**[3,7,8], **Peter J. Campbell**[2], and **Don W. Cleveland**[1]

[1]Ludwig Institute for Cancer Research; Department of Cellular and Molecular Medicine, University of California San Diego School of Medicine, La Jolla, California, USA

[2]Wellcome Sanger Institute, Wellcome Genome Campus, Hinxton, Cambridgeshire, CB10 1SA, UK

[3]Whitehead Institute for Biomedical Research, Cambridge, Massachusetts, USA

[4]University College London Cancer Institute, London, WC1E 6DD, UK

[5]Department of Histopathology, Royal National Orthopaedic Hospital NHS Trust, Stanmore, Middlesex, HA7 4LP, UK

[6]Department of Paediatrics, University of Cambridge, Cambridge, CB2 0QQ, UK

[7]Howard Hughes Medical Institute, Whitehead Institute for Biomedical Research, Cambridge, Massachusetts, USA

[8]Department of Biology, Massachusetts Institute of Technology, Cambridge, Massachusetts, USA

[9]Present address: Department of Pathology, University of Texas Southwestern Medical Center, Dallas, Texas, USA

Abstract

Cancer genomes are frequently characterized by numerical and structural chromosomal abnormalities. Here we integrated a centromere-specific inactivation approach with selection for a conditionally essential gene, a strategy termed 'CEN-SELECT', to systematically interrogate the structural landscape of missegregated chromosomes. We show that single-chromosome missegregation into a micronucleus can directly trigger a broad spectrum of genomic

Editorial Summary:
Cytogenetic and whole-genome sequencing analyses using CEN-SELECT show that mitotic segregation errors generate a broad spectrum of chromosomal aberrations that recapitulate the complex structural features of cancer genomes.

rearrangement types. Cytogenetic profiling revealed that missegregated chromosomes exhibit 120-fold higher susceptibility to developing seven major categories of structural aberrations, including translocations, insertions, deletions, and complex reassembly through chromothripsis coupled to classical non-homologous end joining. Whole-genome sequencing of clonally propagated rearrangements identified random patterns of clustered breakpoints with copy-number alterations resulting in interspersed gene deletions and extrachromosomal DNA amplification events. We conclude that individual chromosome segregation errors during mitotic cell division are sufficient to drive extensive structural variations that recapitulate genomic features commonly associated with human disease.

Alterations in chromosome structure are pervasive in human cancers[1,2] and define a disease group known as genomic disorders[3–5]. These abnormalities can comprise a continuum of complexity, ranging from simple arm-level deletions to intricate networks of rearrangements connecting multiple chromosomes[6–10]. Tumors frequently harbor one or more forms of structural genomic rearrangements, which can underlie disease pathogenesis by altering DNA copy-numbers[11], reshuffling linear DNA sequences[10,12–15], and/or perturbing regulatory architecture[5,16–20]. Cancer genome sequencing has recently uncovered complex structural changes that previously escaped detection by conventional cytogenetics, including chromothripsis – localized rearrangements from the catastrophic shattering of individual chromosomes and subsequent re-stitching in haphazard order[21].

Chromosomes are constantly under assault from intrinsic and extrinsic sources of DNA double-strand breaks (DSBs)[7,22–25], although these challenges are often counteracted by DNA damage repair mechanisms to maintain genomic integrity. Errors in mitotic cell division have emerged as a potent source of endogenous DSBs inflicted onto missegregated chromosomes[26]. Improper chromosome segregation causes numerical aneuploidy and has recently been linked to structural anamolies. For instance, missegregated chromosomes can generate unbalanced translocations when damaged in the cytokinetic furrow[27], acquire arm-level segmental imbalances[28,29], or alternatively, become encapsulated into abnormal structures called micronuclei.

Micronuclei act as a spatially restricted compartment for DSB accumulation during interphase[30,31] with fragmentation of the micronucleated chromosome during the following mitosis[30,32,33]. Although the establishment of a genetically heritable, clonally rearranged human chromosome derived from these events has not been experimentally achieved, chromosomes within micronuclei can acquire localized rearrangement junctions in the next cell cycle[34] resembling chromothriptic-like signatures from cancer genomes[21]. Examples of chromothripsis involving multiple chromosomes and in combination with translocations have been identified in somatic[21,35–37] and inherited[5,38–42] cases, demonstrating that chromothriptic alterations can include events more diverse than rearrangements restricted to an individual chromosome. Despite its prevalence in disease, it remains unknown whether the spectrum of simple and complex genomic rearrangements can be initiated by a unifying mechanism.

We previously established a somatic human cell-based approach to selectively inactivate the Y chromosome centromere by using a gene replacement strategy to rapidly exchange the

centromere-specific histone H3 variant CENP-A with a loss-of-function chimeric mutant, which supports ongoing function of all centromeres except for the Y chromosome[33]. Centromere inactivation caused chromosome-specific missegregation into micronuclei, triggering whole-chromosome shattering during the subsequent mitosis coupled with efficient chromosome loss[33]. To explore the structural rearrangement landscape of missegregated chromosomes, we now develop CEN-SELECT – a strategy combining centromere inactivation-induced chromosome shattering with a drug selection marker engineered into the Y chromosome, which otherwise lacks somatically essential genes. The resulting chromosomal byproducts are therefore unbiased from constraints typically imposed by autosomal gene-dosage effects. Implementing this approach with comprehensive cytogenetic and whole-genome sequencing (WGS) analyses, we show that mitotic segregation errors directly generate a broad spectrum of chromosomal aberrations that reconstruct the complex structural features of cancer genomes.

RESULTS

Development of the CEN-SELECT system in diploid human cells

To induce mitotic errors and identify cells maintaining the missegregated chromosome, we combined a Y centromere-specific inactivation strategy[33] with a Y chromosome-encoded selection marker, an approach we call CEN-SELECT (Fig. 1a). We started with p53-inactivated DLD-1 colorectal cancer cells that are chromosomally stable (46,XY) and carry one disrupted *CENPA* allele with the second allele modified to encode CENP-A fused to an EYFP-linked auxin-inducible degron (AID) tag (CENP-A$^{EYFP-AID/-}$)[33]. Addition of the auxin hormone indole-3-acetic acid (IAA) activates a constitutively expressed E3 ubiquitin ligase (osTIR1) to induce rapid CENP-A$^{EYFP-AID}$ degradation[43,44]. CRISPR/Cas9-mediated genome editing was used to insert a neomycin-resistance gene (*Neo^R*) (Supplementary Fig. 1a,b), which confers survival in the presence of the antibiotic G418, at the Y-chromosome AZFa locus located ~2.5Mb from the centromere on proximal Yq11.221[45]. Correctly targeted clones were identified (Supplementary Fig. 1b,c), and a single-copy, doxycycline (DOX)-inducible wild-type CENP-A (CENP-A^{WT}) or chimeric mutant carrying a histone H3 carboxy-terminal tail substitution (CENP-A$^{C–H3}$) was integrated at a defined FRT site. Replacement of CENP-A$^{EYFP-AID}$ with chimeric CENP-A$^{C–H3}$ supports functional kinetochore assembly at the centromere of all chromosomes except for the Y centromere[33], which lacks CENP-B binding sequences[46]. Genetic modifications and cell cloning steps are outlined in Supplementary Fig. 1a.

Over half (59%) of cells underwent expected loss of the Y chromosome (LOY) (Fig. 1b) within three days of centromere inactivation induced by DOX/IAA addition, as determined by interphase fluorescent *in situ* hybridization (FISH) with Y centromere-targeting DNA probes (CEN-Y). Consistent with increased mitotic errors, the Y chromosome was encapsulated within micronuclei in 56% of cells that retained it – a ~100-fold increase over untreated cells (Fig. 1c,d).

Despite loss of kinetochore function, Y centromere identity is epigenetically preserved by CENP-A$^{C–H3}$-assembled chromatin[33]. We next determined whether inactivated Y centromeres could be reactivated following the removal of DOX/IAA. Endogenous CENP-

A$^{EYFP-AID}$ returned to its initial steady-state level within 3–4 days of drug washout and accompanied by a corresponding decline in CENP-A$^{C–H3}$ synthesis (Supplementary Fig. 2a). Reaccumulated CENP-A$^{EYFP-AID}$ incorporated into centromeric chromatin in interphase and mitotic chromosomes, including the Y chromosome (Supplementary Fig. 2b–d), consistent with Y centromere reactivation, and the proportion of cells containing micronuclei approached baseline.

We next used transient Y centromere inactivation coupled with selection for *Neo^R* gene retention (Fig. 1e). While transient replacement of CENP-A$^{EYFP-AID}$ with CENP-A$^{C–H3}$ alone had no effect on clonogenic growth from single cells, its combination with G418 selection sharply reduced survival by ~89% (Fig. 1f,g). Inspection of G418-resistant populations by FISH revealed that >90% of recovered cells scored positive for retention of the Y chromosome, the vast majority (98%) of which were positioned within the main nucleus (Fig. 1h,i), consistent with centromere reactivation. Additionally, there was no effect on the viability of control cells expressing CENP-A^{WT} treated in parallel (Fig. 1h,i). Thus, CEN-SELECT can experimentally identify cells carrying chromosomes previously exposed to high frequency missegregation into micronuclei.

Release of damaged micronuclear chromatin during mitosis

Micronuclei are intrinsically prone to acquiring DSBs[30,31,33]. Consistent with this, micronuclei produced by Y centromere inactivation recruited components involved in the DNA damage response, including the MRE11-RAD50–NBS1 (MRN) complex (Supplementary Fig. 3a) that is critical for DSB recognition and signaling. Two ATM kinase substrates, H2AX[47] and NBS1[48,49], were also readily phosphorylated (S139 and S343, respectively) within most micronuclei examined. By contrast, whereas the 53BP1 DNA repair factor[50,51] was rapidly recruited to DSB sites induced by chemotherapeutic agents in the major nucleus, micronuclear DSBs failed to actively recruit or retain 53BP1 (Supplementary Fig. 3b), in accordance with previous findings[52], suggesting that micronuclear DNA damage developing during interphase can persist unrepaired into the next mitosis.

Live-cell imaging of nuclear and micronuclear membranes fluorescently labeled with lamin A–GFP revealed that 6.4% of micronuclei (*n*=140, pooled from three experiments) exhibited abnormal nuclear envelope breakdown (NEBD) throughout mitosis (Supplementary Videos 1–2). Micronuclear NEBD kinetics were next assessed by time-lapse microscopy of semi-permeabilized interphase cells treated with mitotic *Xenopus* egg extracts to trigger NEBD[53,54] (Supplementary Fig. 4a–c). Extract-induced nuclear and micronuclear NEBD kinetics were identical in most cells (Supplementary Fig. 4d,e), while in a subset (14%, *n*=51) the micronuclear envelope only partially disassembled and at reduced rate (Supplementary Fig. 4e–g). Thus, whereas partially-disassembled micronuclei can persist for another cell cycle, most micronuclei enter mitosis with timely NEBD, promoting further chromosome missegregation[55] and/or the reincorporation of damaged chromatin into daughter cell nuclei after mitotic exit[30].

Mitotic errors drive widespread structural rearrangements

To test whether chromosome segregation errors directly provoke gross chromosomal rearrangements, Y chromosome paint probes were hybridized to metaphase spread preparations. A majority (59±8%, 92/153 metaphases) of cells examined from CEN-SELECT harbored at least one type of Y-specific structural change (Fig. 2a) with different alterations occurring in each cell (described below). Structural rearrangements were undetectable from 94 control metaphases rescued with CENP-A[WT] and at <1% frequency (1/122 metaphases) in G418-resistant cells without centromere inactivation (Fig. 2a), consistent with a low spontaneous rearrangement rate.

To confirm that rearrangements did not result from selection for rare cells with pre-existing abnormalities, three independent clones were isolated that carried a cytogenetically normal Y chromosome (Supplementary Fig. 1a). Each clone underwent efficient LOY following centromere inactivation (Supplementary Fig. 1d). Y chromosome rearrangement frequencies were elevated in each clone following CEN-SELECT, supporting that the majority of rearrangements were generated *de novo* rather than selection for pre-existing alterations (Fig. 2a). Across the parental cells and clones, CEN-SELECT produced Y chromosome rearrangements at a frequency >2 orders-of-magnitude higher than G418 selection without centromere inactivation (139/297 metaphases versus 1/258 metaphases, respectively) (Fig. 2a). CEN-SELECT did not affect the low rearrangement frequency (1.4%, 2/144 metaphases) of a control autosome (chromosome 14), as determined using chromosome-paint probes, and rearrangements between the Y and chromosome 14 were observed at a frequency (4%, 1/24 Y-translocations) expected by chance (~4.4% in diploid cells). One clone (#1) was selected for subsequent efforts as it was completely haploid for the Y under untreated conditions (*n*=45 metaphases) and had a Y chromosome rearrangement frequency closely matching the parental clone after CEN-SELECT.

Rearrangements recapitulate a diverse SV landscape

To visualize the types of structural rearrangements generated by CEN-SELECT, we designed a metaphase FISH-based assay utilizing two DNA probe sets that distinctly labeled both halves of the Y chromosome (Fig. 2b). A set of green paint probes hybridized to the euchromatic portion of the male-specific region of the Y (MSY) spanning Yp and proximal Yq[56], and another set of red probes (41H10) hybridized to the repetitive, heterochromatic array on distal Yq (YqH). These probe sets produced a characteristic morphology when hybridized to control metaphases, enabling routine discrimination between normal (Fig. 2c) and derivative Y chromosomes.

Cytogenetic inspection of 200 Y chromosomes exhibiting microscopic abnormalities revealed seven major categories of diverse inter- and intra-chromosomal structural alterations (Fig. 2d,3a), including end-fusions, translocations, insertions, complex rearrangements, inversions (Supplementary Fig. 5), isodicentrics, and deletions (see Supplementary Note for detailed descriptions of each type). Derivative chromosomes consisting of multiple rearrangement types were also observed, exemplified by seven cases of complex aberrations combined with translocations (Fig. 3a).

To determine whether chronic centromere inactivation would influence the spectrum of rearrangement types, cells were continuously passaged with G418 alone or under CEN-SELECT conditions (Supplementary Fig. 6a). Whereas cell-doubling rates remained steady under G418 selection, CEN-SELECT cells displayed reduced growth rates during early passages (Supplementary Fig. 6b,c), reflecting competition between proliferating Y chromosome-positive cells and LOY cells undergoing cell death. Proliferation rate accelerated after p4, approaching baseline growth as Y chromosome-positive cells began outcompeting LOY cells (Supplementary Fig. 6c,d). FISH analysis revealed a passage-dependent reduction in Y chromosome fragmentation with a corresponding enrichment in Y chromosome rearrangements that eventually relocated to the nucleus (Supplementary Fig. 6d,e). At the sixth passage, >97% of metaphases (*n*=43) harbored 1–3 copies of a normal or rearranged Y chromosome. Cytogenetic profiling of 201 derivative chromosomes obtained from this final passage detected heterogeneous rearrangement types similar to transient CEN-SELECT (Fig. 3a), but with a notable shift towards more inter-chromosomal rearrangements (Fig. 3b). A possible ring chromosome was also detected (1/401 derivative chromosomes), as well as another uncharacterized rearrangement (Supplementary Fig. 6f). Thus, mitotic chromosome segregation errors trigger a wide spectrum of rearrangements that frequently recapitulate cancer-associated structural alterations.

Rearrangement frequency and specificity through NHEJ repair

We next compared rearrangements generated by CEN-SELECT to two established sources of structural aberrations: DNA damage induced by ionizing radiation (IR) (Supplementary Fig. 7a,b) and random chromosome segregation errors (Supplementary Fig. 7c,d) caused by spindle assembly checkpoint (SAC) inactivation[27,57]. Following the G418 selection procedure, frequencies of *de novo* structural abnormalities affecting four autosomes or both sex chromosomes were measured from 1,968 metaphases (Supplementary Fig. 7e–g). IR caused an expected dose- and chromosome length-dependent increase in rearrangements (Fig. 4a, Supplementary Fig. 7h), whereas SAC inactivation produced modest levels of structural aberrations that weakly correlated with chromosome size (Fig. 4a). In contrast, CEN-SELECT generated Y chromosome-specific rearrangements at a frequency comparable to rearrangements on a single autosome from sublethal IR doses (Fig. 4a), demonstrating that CEN-SELECT achieves efficient rearrangements specifically on chromosomes undergoing increased missegregation rates.

With the exception of terminal deletions, the observed rearrangement products required at least one DNA joining event between two broken chromosome ends. To test the involvement of the two distinct DSB end-joining pathways [classical non-homologous end joining (NHEJ) and alternative end joining (alt-EJ)], each was transiently suppressed by RNAi-mediated co-depletion of LIG4/DNA-PK or LIG3/PARP1, respectively[26] (Fig. 4b). Cytogenetic assessment revealed that inhibition of NHEJ, but not alt-EJ, markedly reduced Y chromosome rearrangement frequencies in the majority of G418-resistant cells (Fig. 4c) – 94% of which harbored a Y chromosome without visible defects (149/159 metaphases). A complementary approach confirmed this, with NHEJ-deficiency conferring clonogenic sensitivity to G418 selection (Fig. 4d), consistent with the failure to reassemble a functional *Neo*[R]-encoding Y chromosome. These data support classical NHEJ as the major DSB repair

mechanism facilitating rearrangement formation on missegregated chromosomes in human cells.

Sequencing of stable and complex genomic rearrangement events

The structural rearrangement landscape of derivative chromosomes produced by CEN-SELECT was next determined at high-resolution by WGS. Single-cell derived subclones were isolated (Fig. 5a) from sustained CEN-SELECT populations that harbored a rearranged Y chromosome within the main nucleus (Supplementary Fig. 6d–e). Metaphase FISH revealed that 22/40 clones carried distinct, clonal Y chromosome rearrangements (Fig. 5b) spanning the diverse spectrum observed in the bulk population (Fig. 3b). Five clones had inter-chromosomal translocations involving the Y with complex patterns of intra-chromosomal rearrangements exhibiting overlapping FISH signals between the MSY/YqH regions (Fig. 5c). Metaphase FISH determined that >95% of cells within each clone propagated the same derivative chromosome even after long-term continuous passage without G418 (Fig. 5d,e), demonstrating that, in the absence of selective pressure, these chromosomes were stably heritable without further changes.

To identify *de novo* structural variants (SVs) and DNA copy-number alterations, the parental DLD-1 clone and 20 derived clones (Fig. 5b) were subjected to paired-end WGS (35.7x mean depth). A control clone carrying a normal Y chromosome (PD37303a) is shown in Fig. 6a, and a summary of cytogenetics and WGS data for each clone is provided in Supplementary Table 1. The frequency of Y chromosome-specific SVs per Mb sequence was enriched ~21-fold compared to the mean of individual autosomes, and the total number of SVs otherwise scaled by chromosome size (Supplementary Fig. 8a,b). We note that these measurements likely underestimate the number of Y chromosome SVs since rearrangements involving reference assembly gaps, including the repetitive YqH region, were excluded from SV analyses, although such junctions were evident by MSY copy-number changes without an associated SV call. The rearrangement partner was identified by WGS for seven clones – each validated by metaphase FISH (Supplementary Fig. 9).

Reconstructing 71 Y-specific intra-chromosomal rearrangement breakpoints revealed that the majority of junctions lacked microhomology beyond a frequency expected by chance from random simulations (Supplementary Fig. 8c; Online Methods). Among these junctions, seven contained 3bp of microhomology and two had 4bp (Supplementary Fig. 8d), consistent with predominant NHEJ-dependent ligation with minimal alt-EJ involvement. Junctions with 2bp of non-templated insertions were also observed within 32% of junctions (23/71) with a median length of 13.5bp and maximum length of 94bp (Supplementary Fig. 8d). Junction sequences with microhomology tracts and long insertions are provided in Supplementary Table 2. Additionally, measurements of intra-DSB distance between consecutive breakpoints indicated that a majority (76%, n=228) of chromosome fragments were <1Mb in size with a median length of 300kb (Supplementary Fig. 8e).

Chromothripsis coupled to inter-chromosomal rearrangements

WGS identified 13 clones with intra-chromosomal rearrangements of the Y chromosome, at least nine of which harbored the canonical signatures of chromothripsis (Fig. 6b–d;

Supplementary Fig. 10), including oscillating copy-number states and clustered breakpoint patterns randomly distributed across the four possible orientations (Supplementary Fig. 8a). Similar complex rearrangements were not observed on other chromosomes. Super-resolution visualization of metaphase chromosomes revealed that complex rearrangements produced intricately-linked FISH patterns with interspersed euchromatic and heterochromatic segments (Fig. 6b). Copy-number profiling further identified short deletions interspersed along the chromosome, a hallmark of chromosome shattering followed by the loss of DNA fragments, and copy-number increases at multiple loci (Fig. 6b–d; Supplementary Fig. 10), indicative of DNA replication errors and/or co-fragmentation of sister chromatids. Oscillations across three, sometimes more, copy-number levels were also observed, patterns suggesting the simultaneous involvement of both sister chromatids in the chromothriptic event[58]. Indeed, as previously shown[33], centromere-inactivated chromosomes occasionally underwent non-dysjunction during mitosis and entrapped both chromatids into the same micronucleus.

Sequencing of two distinct clones resolved independent simple or complex events involving interstitial insertion of Y chromosome fragments into different chromosome 1 arms (Fig. 6e,f). FISH analysis revealed that one (PD37306a) had distinct separation between Y and chromosome 1p sequences, as indicated by an apparent gap using a chromosome 1 painting probe (Fig. 6g). By contrast, another (PD37313a) carried co-localized chromosome 1 and MSY FISH signals (Fig. 6h). PD37313a was determined by WGS to contain a series of shuffled Y chromosome sequences juxtaposed between a *de novo* duplicated segment located on chromosome 1q (Fig. 6f), consistent with chromothriptic fragments inserted into a tandem duplication site, which could arise from stalled replication forks[59].

Hypermutation hotspots were also observed near five chromothriptic junctions (Supplementary Fig. 8f), indicative of kataegis co-occurring with chromosomal rearrangements[60]. These regions comprised strictly C>T mutations with an intermutation distance of <1kb. Kataegic events occurred in proximity to Y-Y breakpoints associated with an SV call (130bp–6.5kb) or binned copy-number change (61–109kb) and were otherwise not observed elsewhere throughout the genome. Interphase DNA bridges[61] containing Y chromosome sequences were undetectable across all CEN-SELECT passages (Supplementary Fig. 6d), supporting micronucleus-mediated origins underlying these kataegis signatures.

We further identified complex Y chromosome rearrangements from an independent cohort of 3/18 male osteosarcomas interrogated by WGS[62], including chromothripsis in a 10-year-old child (PD7193a) (Supplementary Fig. 11a–c). The architecture of these rearrangements resembled those generated by CEN-SELECT, including complex intra- and inter-chromosomal rearrangements accompanied by oscillating copy-number patterns. Similar molecular features were also observed at reconstructed breakpoint junctions (Supplementary Fig. 11d–f). These examples provide proof-of-principle evidence that such rearrangements occur in the context of human cancer, although the degree to which mitotic errors contributes to somatic rearrangements in different cancer types warrants further investigation.

Consequences of chromothriptic DNA copy-number alterations

We next examined how structural rearrangements provoked gene inactivation by mapping gene copy-number states along the Y chromosome. Analysis of 213 well-mapped Y-linked genes and pseudogenes revealed widespread deletions scattered across regions of the initially missegregated chromosome, including five clones with >65% gene loss and eight harboring less frequent (0.5–37%) deletions (Fig. 7a,b). The genomic loci of two Y-encoded genes broadly expressed in somatic cells, *KDM5D* and *EIF1AY*, were inspected at greater resolution. Among the 20 sequenced clones, five carried a structural deletion in either gene and three exhibited co-deletions in both (Supplementary Fig. 12a,b). RT-PCR analysis verified that these genes were not expressed in the corresponding clones (Supplementary Fig. 12c) and provided further evidence that these derivative chromosomes were transcriptionally functional beyond *Neo^R* expression. Thus, in contrast to whole-chromosome aneuploidy that alters gene-dosage across the missegregated chromosome, complex rearrangements arising from chromosome missegregation deletes a subset of interspersed genes through copy-number alterations (Fig. 7c).

Clone PD37310a was resistant to G418 selection despite lacking a cytogenetically-detectable Y chromosome when hybridized to painting probes. WGS revealed that the majority of the Y was lost except for a ~0.9Mb segment surrounding the *Neo^R* marker at Yq11.221 (Fig. 7d). Cytogenetics with FISH probes targeting this locus (RP11–113K10) showed that this region spatially manifested as small fragments of extrachromosomal DNA (ecDNA) (Fig. 7e) reminiscent of cancer-associated double-minute chromosomes[63,64]. PD37310a cells, but not parental controls, heterogeneously maintained multiple copies of this sequence (Fig. 7f), demonstrating that chromosome shattering induced by mitotic errors could elicit ecDNA production – consistent with observations in chromothriptic tumors[21,65]. The head-to-head and tail-to-tail orientation of the two rearrangement junctions (Fig. 7d) suggested that the ecDNA structure was produced from three DSBs that generated two fragments (509kb and 385kb in length), followed by an inversion of one fragment and subsequent re-ligation between the four available ends (Fig. 7g,h).

DISCUSSION

Here we show that chromosomal instability can initiate stable and diverse structural rearrangements that span the spectrum of complexity observed in cancers and genomic disorders, expanding the catalogue of possible genomic rearrangement types caused by cell division errors. Missegregated chromosomes are frequently encapsulated into micronuclei that assemble dysfunctional nuclear envelopes[31,66]. The ensuing loss of nucleocytoplasmic compartmentalization throughout interphase triggers micronucleus-specific DSBs that persist unrepaired into mitosis. These DSBs subsequently resolve into highly fragmented chromatin during mitotic entry[30,32,33] that reintegrates into daughter cell genomes after mitotic exit[30,34].

Following the completion of mitosis, inherited chromosome fragments are deposited into a functional G1-phase nucleus to initiate the reassembly process by activating the DNA damage response. Because NHEJ is temporally active during early cell cycle phases, we propose that the NHEJ machinery engages these fragments for re-ligation, triggering both

intra- and inter-chromosomal rearrangements depending on the availability and/or spatial proximity of compatible DNA ends. We show that inhibiting NHEJ suppresses chromosome rearrangement formation (Fig. 4c), and the breakpoint junctions of re-ligated fragments do not utilize sequence homology beyond that expected from random chance (Supplementary Fig. 8c,d). Microhomology-mediated repair through alt-EJ, however, may be involved in processing remaining DSBs that persist into S-/G2-phases when end-resection is operative[67]. Whereas recombination-dependent DSB repair preserves sequence integrity at breakpoint junctions, end joining-mediated repair can generate mutagenic indels. Although the mechanisms linking rearrangements with kataegis remain unclear, our data suggest that some breakpoints (Supplementary Fig. 8f) are likely reassembled through an intermediate step consisting of exposed single-stranded DNA processed by APOBEC enzymes[68].

Use of CEN-SELECT has generated functional and genetically stable chromosomes that have undergone chromothripsis and which persist over multiple cell cycles even without continued selection. Importantly, apart from the requirement during selection to retain Neo^R, the sparse gene content and lack of essential genes on the Y chromosome eliminates constraints on the possible 'solution space' of SV configurations that can arise, allowing for an unbiased view of the rearrangement landscape driven by mitotic errors. For instance, complex reassembly events retained multiple segments of Y-sequences despite no selective pressure for its maintenance (Figure 6, Supplementary Figure 10). At a minimum, the reconstitution of a stable derivative chromosome requires the re-stitching of fragments that include an epigenetically-active centromere with two end-capping telomeres. Because the majority of DNA fragments produced from micronucleus-mediated chromosome shattering are acentric[33], retention of any essential chromosomal element(s) may be facilitated through rearrangements with a normally segregating, non-homologous chromosome harboring a spontaneous DSB, thereby reacquiring the capacity for its faithful inheritance.

Here we exploited unique features of the Y chromosome to reconstruct the mechanisms and consequences of genomic aberrations[69]. Although a contribution from underlying experimental factors (Y-specific features, resistance gene position) or genetic background (*TP53* status, MMR-deficiency) cannot be formally excluded, we anticipate that the observations reported here are generalizable across chromosomes. We provide evidence that chromothriptic rearrangements can focally delete genes located on missegregated chromosomes (Fig. 7a,b), findings with implications for tumor suppressor gene loss in cancer. Such deletions likely arise through the unequal distribution of DNA fragments during mitosis[34] and from inherited fragments that either failed to participate in the chromosome rearrangement event (Fig. 7c) or stochastically reassembled into an unstable configuration. Conversely, copy-number increases can be generated through DNA replication errors (e.g., template-switching), or in more extreme cases, the ligation of fragment ends to produce autonomously-replicating, circular ecDNA structures lacking centromeres and telomeres, which act as a frequent mode of oncogene amplification in cancer[63,64]. Indeed, the ecDNA carried by clone PD37310a co-amplified 14 additional genes within the vicinity of the selection marker (Fig. 7h). The short fragments generated by chromosome shattering (Supplementary Fig. 8e) may be conducive for ecDNA production to drive gene amplification events associated with tumorigenesis and/or chemotherapeutic-resistance.

Rearrangements arising from chromosome shattering are likely frequent in chromosomally unstable cells exhibiting high rates of chromosome segregation errors, especially those deficient in the p53 checkpoint[28,29,65]. The majority of random chromosome products formed from these events, however, is probably deleterious or confers no positive advantage. In rarer instances, chromosome shattering may trigger a series of rearrangements in which a 'perfect storm' of genetic lesions are created through DNA copy-number alterations, disruptive breakpoints, and/or mutations to enable clonal and oncogenic selective advantages[70]. Such catastrophic events can operate as a punctuated mutational mechanism to rapidly remodel the cancer genome[26,71].

METHODS

Cell culture and reagents

T-REx Flp-In DLD-1 cells were cultured in Dulbecco's modified Eagle's medium (DMEM, Thermo Fisher) containing 10% tetracycline-free fetal bovine serum (FBS) (Omega Scientific) and 100 U/mL penicillin-streptomycin. hTERT-immortalized RPE-1 cells were cultured in DMEM/F12 (Thermo Fisher) supplemented with 10% FBS, 100 U/mL penicillin-streptomycin, 2 mM L-glutamine, and 0.348% sodium bicarbonate. All cells were maintained at 37°C under 5% CO_2 and atmospheric oxygen.

Doxycycline (DOX) and indole-3-acetic acid (IAA) were purchased from Sigma, dissolved in cell culture-grade water, and used at 1 μg/mL and 500 μM, respectively. Where indicated, DOX/IAA washout was performed by two washes in PBS followed by addition of growth medium. The Mps1 inhibitor reversine (Santa Cruz) was dissolved in DMSO and used at the indicated concentrations. Geneticin (G418 Sulfate) and hygromycin (Thermo Fisher Scientific) were used at selection concentrations of 300 μg/mL and 200 μg/mL, respectively. DLD-1 siRNA transfections were conducted with Lipofectamine RNAiMAX reagent (Thermo Fisher Scientific) using characterized siRNAs (GE Healthcare Dharmacon) as previously described[33].

Genome engineering and modifications

T-REx Flp-In DLD-1 cells, which were previously modified to carry a heterozygous CENP-A EYFP-AID fusion tag (CENP-A[EYFP-AID/−]) and stably express osTIR1[33], were used as the starting material for all DLD-1 experiments. To integrate a selectable marker into the Y chromosome by CRISPR editing, target sequences for guide RNAs were selected using CRISPR Design Tool (see URLs). An oligo (5'-AACACTTCTCTAGCACGATT-3') encoding a guide RNA targeting the Y chromosome AZFa locus (target coordinate 12,997,776 using GRCh38 reference assembly) was cloned into the Bbs1 restriction site of the pSpCas9(BB)-2A-GFP vector (PX458, Addgene #48138) and co-transfected into DLD-1 CENP-A[EYFP-AID/−] cells with a synthesized pUC57-based donor vector containing an EF1α promoter driving the neomycin resistance gene (*Neo[R]*) flanked by 450 bp left and right AZFa homology arms (GenScript). Following transfection using X-tremeGENE 9 DNA Transfection Reagent (Sigma-Aldrich), cells were selected with G418 for 20 days and plated by limiting dilution into 96-well plates. G418-resistant, single cell-derived clones were expanded and screened by PCR for targeted insertion of *Neo[R]* into the AZFa locus using a

forward primer located outside the left homology arm and a reverse primer located within the EF1α promoter. A forward primer sitting inside the left donor homology arm with the same reverse primer were used as a control, as well as primers amplifying the sY1250 sequence-tagged site (STS). All PCR primer sequences are provided in Supplementary Table 3. Clones identified by PCR were confirmed to harbor a single copy of a morphologically normal-appearing Y chromosome using DNA FISH on metaphase spreads.

Following Y chromosome editing, CENP-A WT or C–H3 rescue constructs were integrated into the Flp-In locus, as previously described[33]. Briefly, cells were co-transfected with pOG44 and pcDNA5 constructs carrying the indicated CENP-A rescue gene using X-tremeGENE 9 DNA Transfection Reagent (Sigma-Aldrich), and successfully targeted cells with correct integration were selected with hygromycin.

To generate cells with fluorescently-labeled nuclear envelopes, DLD-1 and RPE-1 H2B–mRFP cells were transduced with retroviruses packaged in 293GP cells to stably express pBABE-puro-GFP-wt-lamin A (Addgene #17662). Fluorescent cells were isolated by flow cytometry on a BD FACSAria II Cell Sorter (UCSD Stem Cell Core).

Cell growth measurements

For colony formation assays, trypsinized cells were pelleted, diluted as needed, and seeded at low density into 10-cm^2 or 6-well plates for up to two weeks. Cells were fed with fresh growth medium each week. Cells were fixed with 100% methanol at room temperature, incubated in 0.5% crystal violet, 25% methanol solution with gentle agitation for 30 minutes, and washed with water. To account for expected ~10-fold differences in clonogenic growth in Fig. 4d, all DOX/IAA-treated conditions were seeded at a 10-fold higher cell density than control non-DOX-IAA-treated cells to yield a comparable number of colonies at time of fixation. For quantification of cell proliferation rates, 1×10^6 cells were seeded into 10-cm^2 plates and total cell numbers were counted using a hemacytometer every 5 days. 1×10^6 cells were re-seeded into new 10-cm^2 plates and repeated for up to 30 days.

Nuclear envelope disassembly assay using Xenopus egg extracts

Interphase and CSF-arrested extracts were prepared from *Xenopus laevis* eggs as described[72]. Crude extracts were supplemented with 250 mM sucrose and aliquots were snap frozen and stored at –80°C. All animal protocols complied with ethical regulations set forth and approved by UC San Diego and the Institutional Animal Care and Use Committee (IACUC). To generate RPE-1 cells with micronuclei by nocodazole washout, RPE-1 H2B–mRFP and lamin A–GFP cells were arrested in mitosis for 6 hours with 100 ng/mL nocodazole (Sigma), harvested by mitotic shake-off, and released into fresh growth medium overnight in 4-well chamberslides. For nuclear envelope disassembly assays, a slightly modified protocol adapted from Mühlhäusser *et al.*[54] and Shankaran *et al.*[73] were closely followed. Briefly, chamberslides were incubated on ice for 5 minutes and washed with cold permeabilization buffer (20 mM Hepes, pH 7.4, 110 mM KoAc, 5 mM MgOAc, 0.5 mM EGTA, 250 mM sucrose) for 5 minutes. Cells were then incubated on ice for 5 minutes in permeabilization buffer containing 40 μg/mL digitonin (Promega) while frozen egg extracts were allowed to thaw on ice. Cells were washed three times with cold permeabilization

buffer for 5 minutes each. 500 μL of thawed egg extracts were added per chamber and cells were imaged on a DeltaVision RT (GE Healthcare) microscope system using a 60x objective with 20×0.2-μm z-sections at 4–6 minute intervals. Time-lapse images were deconvolved and maximum intensity quick projections videos were generated using softWoRx (Applied Precision) program. GFP fluorescent intensities were measured using ImageJ.

Metaphase spread preparation

Subconfluent cell cultures were incubated with 100 ng/mL KaryoMAX (Thermo Fisher Scientific) diluted in fresh growth medium for 4 hours. Cells were trypsinized, pelleted, and slowly resuspended in 0.075 M KCl solution dropwise with gentle vortexing, followed by incubation at 37°C for 6 minutes and addition of 1:6 total volume of pre-chilled Carnoy's fixative (3:1 methanol:acetic acid). Cells were then pelleted, resuspended in pre-chilled Carnoy's fixative, and centrifuged. Cells were resuspended in pre-chilled Carnoy's fixative and stored at −20°C. To prepare metaphase spreads, 10 μL of fixed cell suspensions were dropped onto glass slides and air-dried.

Interphase and metaphase DNA fluorescence in situ hybridization (FISH)

Chromosome paint and centromere enumeration probes were purchased from MetaSystems. Yq heterochromatin (YqH, 41H10) and RP11–113K10 BAC probes were obtained from BACPAC Resources Program, CHORI (see URLs). 41H10 BAC DNA was isolated from 200 mL bacterial cultures using the Plasmid Midi Kit (Qiagen) and labeled with Cy3 label using nick-translation protocol for DNA Polymerase I/Dnase I (Life Technologies). RP11–113K10 BAC DNA was isolated from 50 mL bacterial cultures using the BACMAX DNA Purification Kit (Epicentre), sonicated (Branson Ultrasonics Sonifier S-450), and labeled with TM-rhodamine using a Label IT Nucleic Acid Labeling Kit (Mirus Bio). Labeled BAC probes were resuspended in FITC-labeled Y chromosome paint probes (Metasystems).

To perform FISH on interphase cells, unsynchronized cells cultured in chamberslides were washed with PBS and fixed with Carnoy's fixative for 15 minutes at room temperature. Slides were dehydrated in 80% ethanol and air-dried.

FISH probes were combined as indicated, applied to interphase cells or metaphase spreads on glass slides, and sealed with a coverslip. Samples and probes were co-denatured at 75°C for 2 minutes, followed by sealing with rubber cement and overnight hybridization at 37°C in a humidified chamber. Slides were washed in 0.4x SSC at 72°C for 2 minutes and in 2x SSC, 0.05% Tween-20 at room temperature for 30 seconds. Slides were rinsed in water, stained with DAPI, and mounted in ProLong Gold anti-fade mounting solution.

For quantification of chromosomal rearrangement frequencies, randomly selected metaphases were imaged, manually inspected using the indicated DNA FISH probes, and scored for *de novo* structural chromosomal abnormalities when compared to the parental DLD-1 karyotype.

Immunofluorescence and immuno-FISH

For immunofluorescence, cells seeded on coverslips or chamberslides were fixed with 4% formaldehyde diluted in PBS for 10 minutes and washed with PBS. Cells were then permeabilized with 0.3% Triton X-100, PBS for 5 minutes, washed with PBS, and blocked with Triton Block (0.1% Triton X-100, 2.5% FBS, 0.2 M glycine, PBS). Primary antibodies were diluted in Triton Block and applied to cells for 1 hour at room temperature or overnight at 4°C, followed by three 10-minute washes with 0.1% Triton X-100, PBS. The following primary antibodies were used at 1:1,000 dilution in Triton Block: CENP-A (ab13939, Abcam), GFP (A10262, Invitrogen), phospho-S139 γH2AX (clone JBW301, 05–636, Millipore), and 53BP1 (NB100–304, Novus Biologicals). The following primary antibodies were obtained from GeneTex and used at 1:500 dilution in Triton Block: MRE11 (GTX70212), RAD50 (GTX70228), NBS1 (GTX70222), and phospho-S343 NBS1 (GTX61779). Fluorescence-conjugated secondary antibodies (Thermo Fisher Scientific) were diluted 1:500 in Triton Block and applied to cells for 1 hour at room temperature, followed by three 10-minute washes with 0.1% Triton X-100, PBS and staining with DAPI. Cells were mounted in ProLong Gold anti-fade mounting solution and imaged as described.

For immunofluorescence combined with DNA FISH, the immunofluorescence procedure was performed as described followed by fixation in Carnoy's fixative for 10 minutes at room temperature and dehydration in 80% ethanol for 5 minutes. Samples were then processed for FISH as described.

Fixed and live-cell microscopy

Metaphase FISH images were captured on a DeltaVision Elite (GE Healthcare) microscope system with a 60x objective and 5×0.5-μm z-sections. Maximum intensity quick projections were generated using softWoRx. Immunofluorescence images were captured at 30×0.2-μm z-sections, followed by deconvolution and maximum intensity quick projections using softWoRx. Structured illumination microscopy imaging was performed on metaphase spreads using a DeltaVision OMX SR (GE Healthcare) microscope system with a 100x objective (Olympus PlanApo 1.4 NA) and EMCCD 10 Mhz camera mode. Raw images were reconstructed and aligned for super-resolution using softWoRx with the following Wiener filters: 525 nm, 0.020; 442 nm, 0.020; 600 nm, 0.015.

For live-cell imaging experiments, 1×10^4 cells/well were seeded into CELLSTAR μClear 96-well plates (Greiner Bio-One) and imaged on a Yokogawa CQ1 confocal image cytometer with a 40x objective. To determine mitotic timing and the formation of micronuclei with mitotic checkpoint inactivation, cells were seeded 16 hours prior to staining with 500 nM SiR-DNA (Spirochrome) and treatment with reversine (Santa Cruz) at the indicated concentrations, followed by image acquisition at 5-minute intervals with 5×2-μm z-sections per field. To monitor nuclear envelope breakdown in cells stably expressing lamin A–GFP, micronuclei were induced by 3d DOX/IAA treatment, followed by image acquisition at 5- or 6-minute intervals with 6×1.5-μm z-sections per field. Mean intensity projections were created using ImageJ.

Immunoblotting

Whole-cell extracts were collected in SDS sample buffer and boiled for 10 minutes. Samples were resolved by SDS-PAGE, transferred to PVDF, and blocked with 5% milk in PBST (PBS, 0.1% Tween-20). Primary antibodies against CENP-A (2186, Cell Signaling) and GAPDH (14C10, Cell Signaling) were diluted 1:1,000 and 1:2,000, respectively, in PBST followed by incubation and three 10-minute washes in PBST. Membranes were incubated with HRP-conjugated secondary antibodies diluted 1:4,000 in 5% milk in PBST followed by three 10-minute washes in PBST and exposure to film.

Reverse transcription polymerase chain reaction (RT-PCR)

Total RNA was extracted using a NucleoSpin RNA kit (Machery-Nagel) according to manufacturers' instructions. cDNA libraries were created from 4 μg of total RNA using a High Capacity cDNA Reverse Transcription Kit (Applied Biosystems) with random primers. PCR was conducted using Q5 High-Fidelity polymerase (NEB) with the following reaction conditions: 98°C for 3 minutes, 30 cycles of 98°C for 1 minute, 63°C for 1 minute, and 72°C for 1 minute, followed by 72°C extension for 5 minutes. PCR products were resolved by electrophoresis on a 2% agarose gel and visualized with ethidium bromide. All RT-PCR primer sequences are provided in Supplementary Table 3.

Next-generation DNA sequencing and mapping

Genomic DNA was prepared using a Quick-DNA Plus Kit (Zymo) according to manufacturers' instructions. Sequencing libraries were generated from genomic DNA on robots according to manufacturers' protocols. DNA was sequenced on an Illumina HiSeq X Ten platform to a targeted whole human genome coverage of 30x. Cluster generation and sequencing were performed using the manufacturers' pipelines. Average sequence coverage achieved across all samples was 35.7x (range, 31.4–39.8x) with 151 bp paired-ends and insert size of ~500 bp. Mapping to the human genome was performed using the BWA algorithm[74] BWA-MEM (Version 0.7.8) and genome build hs37d5.

Copy-number and structural variant calling

Copy-number was called using the ascatNgs algorithm[75]. The variant calling pipeline of the Cancer Genome Project, Wellcome Sanger Institute was used to call somatic mutations[76]. The following algorithms with standard settings and no additional post-processing were used: CaVEMan for substitutions and BRASS for rearrangements.

We note that clones harboring Y chromosome end-to-end fusions without additional rearrangements identified by cytogenetics proved uninformative due to the sequence junctions spanning repetitive telomeric sequences. We also note that X-Y translocation calls arose in three clones due to mapping errors, most likely caused by sequence similarities between regions of the X and Y chromosomes. All of these calls mapped to the distal end of Xp, which were confirmed by FISH to be false-positive signals and subsequently removed from the reported sequencing data.

Simulation of random microhomology at breaksites

To simulate the expected frequency of microhomology lengths at breaksites, we used a randomization approach to mimic the sequence context at the actual breaksites identified in our samples. The set of all rearrangement calls were replicated 100x and a random number within the range of −5,000 and 5,000 was added to each breaksite position. The length of homology at the junctions of these simulated breaksite sequences were then measured.

Statistical analysis and reproducibility

Statistical analyses were performed using GraphPad Prism 7.0 software with the tests as described in the figure legends; all P-values were derived from experiments repeated independently at least three times. Error bars represent SEM of at least three independent experiments unless indicated. Figures with representative images were reproduced and obtained from two or more independent experiments.

Reporting summary

Further information is available in the Life Sciences Reporting Summary linked to this article.

Accession Codes

Whole-genome sequencing data have been deposited at the European Genome-phenome Archive (EGA) under accession number EGAD00001004163.

Data availability

The data that support the findings of this study are available from the corresponding authors upon request. Whole-genome sequencing data have been deposited at the European Genome-phenome Archive (EGA) under accession number EGAD00001004163.

URLs

CRISPR Design Tool, http://crispr.mit.edu; BACPAC Resources Program, CHORI, https://bacpacresources.org

Supplementary Material

Refer to Web version on PubMed Central for supplementary material.

ACKNOWLEDGEMENTS

REFERENCES

1. Campbell PJ et al. Identification of somatically acquired rearrangements in cancer using genome-wide massively parallel paired-end sequencing. Nat Genet 40, 722–9 (2008). [PubMed: 18438408]

2. Stephens PJ et al. Complex landscapes of somatic rearrangement in human breast cancer genomes. Nature 462, 1005–10 (2009). [PubMed: 20033038]

3. Carvalho CM & Lupski JR Mechanisms underlying structural variant formation in genomic disorders. Nat Rev Genet 17, 224–38 (2016). [PubMed: 26924765]

4. Liu P et al. An Organismal CNV Mutator Phenotype Restricted to Early Human Development. Cell 168, 830–842 e7 (2017). [PubMed: 28235197]

5. Redin C et al. The genomic landscape of balanced cytogenetic abnormalities associated with human congenital anomalies. Nat Genet 49, 36–45 (2017). [PubMed: 27841880]

6. Bass AJ et al. Genomic sequencing of colorectal adenocarcinomas identifies a recurrent VTI1A-TCF7L2 fusion. Nat Genet 43, 964–968 (2011). [PubMed: 21892161]

7. Yang L et al. Diverse mechanisms of somatic structural variations in human cancer genomes. Cell 153, 919–29 (2013). [PubMed: 23663786]

8. Baca SC et al. Punctuated evolution of prostate cancer genomes. Cell 153, 666–77 (2013). [PubMed: 23622249]

9. Notta F et al. A renewed model of pancreatic cancer evolution based on genomic rearrangement patterns. Nature 538, 378–382 (2016). [PubMed: 27732578]

10. Anderson ND et al. Rearrangement bursts generate canonical gene fusions in bone and soft tissue tumors. Science 361(2018).

11. Cogen PH, Daneshvar L, Metzger AK & Edwards MS Deletion mapping of the medulloblastoma locus on chromosome 17p. Genomics 8, 279–85 (1990). [PubMed: 1979050]

12. Nowell PC The minute chromosome (Phl) in chronic granulocytic leukemia. Blut 8, 65–6 (1962). [PubMed: 14480647]

13. Rowley JD Letter: A new consistent chromosomal abnormality in chronic myelogenous leukaemia identified by quinacrine fluorescence and Giemsa staining. Nature 243, 290–3 (1973). [PubMed: 4126434]

14. de Klein A et al. A cellular oncogene is translocated to the Philadelphia chromosome in chronic myelocytic leukaemia. Nature 300, 765–7 (1982). [PubMed: 6960256]

15. Gao Q et al. Driver Fusions and Their Implications in the Development and Treatment of Human Cancers. Cell Rep 23, 227–238 e3 (2018). [PubMed: 29617662]

16. Northcott PA et al. Enhancer hijacking activates GFI1 family oncogenes in medulloblastoma. Nature 511, 428–34 (2014). [PubMed: 25043047]

17. Zhang X et al. Identification of focally amplified lineage-specific super-enhancers in human epithelial cancers. Nat Genet 48, 176–82 (2016). [PubMed: 26656844]

18. Hnisz D et al. Activation of proto-oncogenes by disruption of chromosome neighborhoods. Science 351, 1454–1458 (2016). [PubMed: 26940867]

19. Weischenfeldt J et al. Pan-cancer analysis of somatic copy-number alterations implicates IRS4 and IGF2 in enhancer hijacking. Nat Genet 49, 65–74 (2017). [PubMed: 27869826]

20. Dixon JR et al. Integrative detection and analysis of structural variation in cancer genomes. Nat Genet (2018).

21. Stephens PJ et al. Massive genomic rearrangement acquired in a single catastrophic event during cancer development. Cell 144, 27–40 (2011). [PubMed: 21215367]

22. Lombard DB et al. DNA repair, genome stability, and aging. Cell 120, 497–512 (2005). [PubMed: 15734682]

23. Lin C et al. Nuclear receptor-induced chromosomal proximity and DNA breaks underlie specific translocations in cancer. Cell 139, 1069–83 (2009). [PubMed: 19962179]

24. Henssen AG et al. PGBD5 promotes site-specific oncogenic mutations in human tumors. Nat Genet 49, 1005–1014 (2017). [PubMed: 28504702]

25. Garaycoechea JI et al. Alcohol and endogenous aldehydes damage chromosomes and mutate stem cells. Nature 553, 171–177 (2018). [PubMed: 29323295]

26. Ly P & Cleveland DW Rebuilding Chromosomes After Catastrophe: Emerging Mechanisms of Chromothripsis. Trends Cell Biol 27, 917–930 (2017). [PubMed: 28899600]

27. Janssen A, van der Burg M, Szuhai K, Kops GJ & Medema RH Chromosome segregation errors as a cause of DNA damage and structural chromosome aberrations. Science 333, 1895–8 (2011). [PubMed: 21960636]

28. Soto M et al. p53 Prohibits Propagation of Chromosome Segregation Errors that Produce Structural Aneuploidies. Cell Rep 19, 2423–2431 (2017). [PubMed: 28636931]

29. Santaguida S et al. Chromosome Mis-segregation Generates Cell-Cycle-Arrested Cells with Complex Karyotypes that Are Eliminated by the Immune System. Dev Cell 41, 638–651 e5 (2017). [PubMed: 28633018]

30. Crasta K et al. DNA breaks and chromosome pulverization from errors in mitosis. Nature 482, 53–8 (2012). [PubMed: 22258507]

31. Hatch EM, Fischer AH, Deerinck TJ & Hetzer MW Catastrophic nuclear envelope collapse in cancer cell micronuclei. Cell 154, 47–60 (2013). [PubMed: 23827674]

32. Kato H & Sandberg AA Chromosome pulverization in human cells with micronuclei. J Natl Cancer Inst 40, 165–79 (1968). [PubMed: 5635016]

33. Ly P et al. Selective Y centromere inactivation triggers chromosome shattering in micronuclei and repair by non-homologous end joining. Nat Cell Biol 19, 68–75 (2017). [PubMed: 27918550]

34. Zhang CZ et al. Chromothripsis from DNA damage in micronuclei. Nature 522, 179–84 (2015). [PubMed: 26017310]

35. Garsed DW et al. The architecture and evolution of cancer neochromosomes. Cancer Cell 26, 653–67 (2014). [PubMed: 25517748]

36. Mitchell TJ et al. Timing the Landmark Events in the Evolution of Clear Cell Renal Cell Cancer: TRACERx Renal. Cell (2018).

37. Cortés-Ciriano I et al. Comprehensive analysis of chromothripsis in 2,658 human cancers using whole-genome sequencing. bioRxiv 333617(2018).

38. Kloosterman WP et al. Chromothripsis as a mechanism driving complex de novo structural rearrangements in the germline. Hum Mol Genet 20, 1916–24 (2011). [PubMed: 21349919]

39. Kloosterman WP et al. Constitutional chromothripsis rearrangements involve clustered double-stranded DNA breaks and nonhomologous repair mechanisms. Cell Rep 1, 648–55 (2012). [PubMed: 22813740]

40. Chiang C et al. Complex reorganization and predominant non-homologous repair following chromosomal breakage in karyotypically balanced germline rearrangements and transgenic integration. Nat Genet 44, 390–7, S1 (2012). [PubMed: 22388000]

41. Weckselblatt B, Hermetz KE & Rudd MK Unbalanced translocations arise from diverse mutational mechanisms including chromothripsis. Genome Res 25, 937–47 (2015). [PubMed: 26070663]

42. Cretu Stancu M et al. Mapping and phasing of structural variation in patient genomes using nanopore sequencing. Nat Commun 8, 1326 (2017). [PubMed: 29109544]

43. Nishimura K, Fukagawa T, Takisawa H, Kakimoto T & Kanemaki M An auxin-based degron system for the rapid depletion of proteins in nonplant cells. Nat Methods 6, 917–22 (2009). [PubMed: 19915560]

44. Holland AJ, Fachinetti D, Han JS & Cleveland DW Inducible, reversible system for the rapid and complete degradation of proteins in mammalian cells. Proc Natl Acad Sci U S A 109, E3350–7 (2012). [PubMed: 23150568]

45. Sun C et al. An azoospermic man with a de novo point mutation in the Y-chromosomal gene USP9Y. Nat Genet 23, 429–32 (1999). [PubMed: 10581029]

46. Masumoto H, Masukata H, Muro Y, Nozaki N & Okazaki T A human centromere antigen (CENP-B) interacts with a short specific sequence in alphoid DNA, a human centromeric satellite. J Cell Biol 109, 1963–73 (1989). [PubMed: 2808515]

47. Burma S, Chen BP, Murphy M, Kurimasa A & Chen DJ ATM phosphorylates histone H2AX in response to DNA double-strand breaks. J Biol Chem 276, 42462–7 (2001). [PubMed: 11571274]

48. Zhao S et al. Functional link between ataxia-telangiectasia and Nijmegen breakage syndrome gene products. Nature 405, 473–7 (2000). [PubMed: 10839544]

49. Wu X et al. ATM phosphorylation of Nijmegen breakage syndrome protein is required in a DNA damage response. Nature 405, 477–82 (2000). [PubMed: 10839545]

50. Schultz LB, Chehab NH, Malikzay A & Halazonetis TD p53 binding protein 1 (53BP1) is an early participant in the cellular response to DNA double-strand breaks. J Cell Biol 151, 1381–90 (2000). [PubMed: 11134068]

51. Anderson L, Henderson C & Adachi Y Phosphorylation and rapid relocalization of 53BP1 to nuclear foci upon DNA damage. Mol Cell Biol 21, 1719–29 (2001). [PubMed: 11238909]

52. Terradas M, Martin M, Tusell L & Genesca A DNA lesions sequestered in micronuclei induce a local defective-damage response. DNA Repair (Amst) 8, 1225–34 (2009). [PubMed: 19683478]

53. Miake-Lye R & Kirschner MW Induction of early mitotic events in a cell-free system. Cell 41, 165–75 (1985). [PubMed: 3888406]

54. Muhlhausser P & Kutay U An in vitro nuclear disassembly system reveals a role for the RanGTPase system and microtubule-dependent steps in nuclear envelope breakdown. J Cell Biol 178, 595–610 (2007). [PubMed: 17698605]

55. Soto M, Garcia-Santisteban I, Krenning L, Medema RH & Raaijmakers JA Chromosomes trapped in micronuclei are liable to segregation errors. J Cell Sci 131(2018).

56. Skaletsky H et al. The male-specific region of the human Y chromosome is a mosaic of discrete sequence classes. Nature 423, 825–37 (2003). [PubMed: 12815422]

57. Santaguida S, Tighe A, D'Alise AM, Taylor SS & Musacchio A Dissecting the role of MPS1 in chromosome biorientation and the spindle checkpoint through the small molecule inhibitor reversine. J Cell Biol 190, 73–87 (2010). [PubMed: 20624901]

58. Li Y et al. Constitutional and somatic rearrangement of chromosome 21 in acute lymphoblastic leukaemia. Nature 508, 98–102 (2014). [PubMed: 24670643]

59. Willis NA et al. Mechanism of tandem duplication formation in BRCA1-mutant cells. Nature 551, 590–595 (2017). [PubMed: 29168504]

60. Nik-Zainal S et al. Mutational processes molding the genomes of 21 breast cancers. Cell 149, 979–93 (2012). [PubMed: 22608084]

61. Maciejowski J, Li Y, Bosco N, Campbell PJ & de Lange T Chromothripsis and Kataegis Induced by Telomere Crisis. Cell 163, 1641–54 (2015). [PubMed: 26687355]

62. Behjati S et al. Recurrent mutation of IGF signalling genes and distinct patterns of genomic rearrangement in osteosarcoma. Nat Commun 8, 15936 (2017). [PubMed: 28643781]

63. Turner KM et al. Extrachromosomal oncogene amplification drives tumour evolution and genetic heterogeneity. Nature 543, 122–125 (2017). [PubMed: 28178237]

64. deCarvalho AC et al. Discordant inheritance of chromosomal and extrachromosomal DNA elements contributes to dynamic disease evolution in glioblastoma. Nat Genet 50, 708–717 (2018). [PubMed: 29686388]

65. Rausch T et al. Genome sequencing of pediatric medulloblastoma links catastrophic DNA rearrangements with TP53 mutations. Cell 148, 59–71 (2012). [PubMed: 22265402]

66. Liu S et al. Nuclear envelope assembly defects link mitotic errors to chromothripsis. Nature 561, 551–555 (2018). [PubMed: 30232450]

67. Truong LN et al. Microhomology-mediated End Joining and Homologous Recombination share the initial end resection step to repair DNA double-strand breaks in mammalian cells. Proc Natl Acad Sci U S A 110, 7720–5 (2013). [PubMed: 23610439]

68. Taylor BJ et al. DNA deaminases induce break-associated mutation showers with implication of APOBEC3B and 3A in breast cancer kataegis. Elife 2, e00534 (2013). [PubMed: 23599896]

69. Ly P & Cleveland DW Interrogating cell division errors using random and chromosome-specific missegregation approaches. Cell Cycle 16, 1252–1258 (2017). [PubMed: 28650219]

70. Mardin BR et al. A cell-based model system links chromothripsis with hyperploidy. Mol Syst Biol 11, 828 (2015). [PubMed: 26415501]

71. Leibowitz ML, Zhang CZ & Pellman D Chromothripsis: A New Mechanism for Rapid Karyotype Evolution. Annu Rev Genet 49, 183–211 (2015). [PubMed: 26442848]

METHODS-ONLY REFERENCES

72. Murray AW Cell cycle extracts. Methods Cell Biol 36, 581–605 (1991). [PubMed: 1839804]

73. Shankaran SS, Mackay DR & Ullman KS A time-lapse imaging assay to study nuclear envelope breakdown. Methods Mol Biol 931, 111–22 (2013). [PubMed: 23027000]

74. Li H & Durbin R Fast and accurate long-read alignment with Burrows-Wheeler transform. Bioinformatics 26, 589–95 (2010). [PubMed: 20080505]

75. Raine KM et al. ascatNgs: Identifying Somatically Acquired Copy-Number Alterations from Whole-Genome Sequencing Data. Curr Protoc Bioinformatics 56, 15 9 1–15 9 17 (2016).

76. Nik-Zainal S et al. Landscape of somatic mutations in 560 breast cancer whole-genome sequences. Nature 534, 47–54 (2016). [PubMed: 27135926]
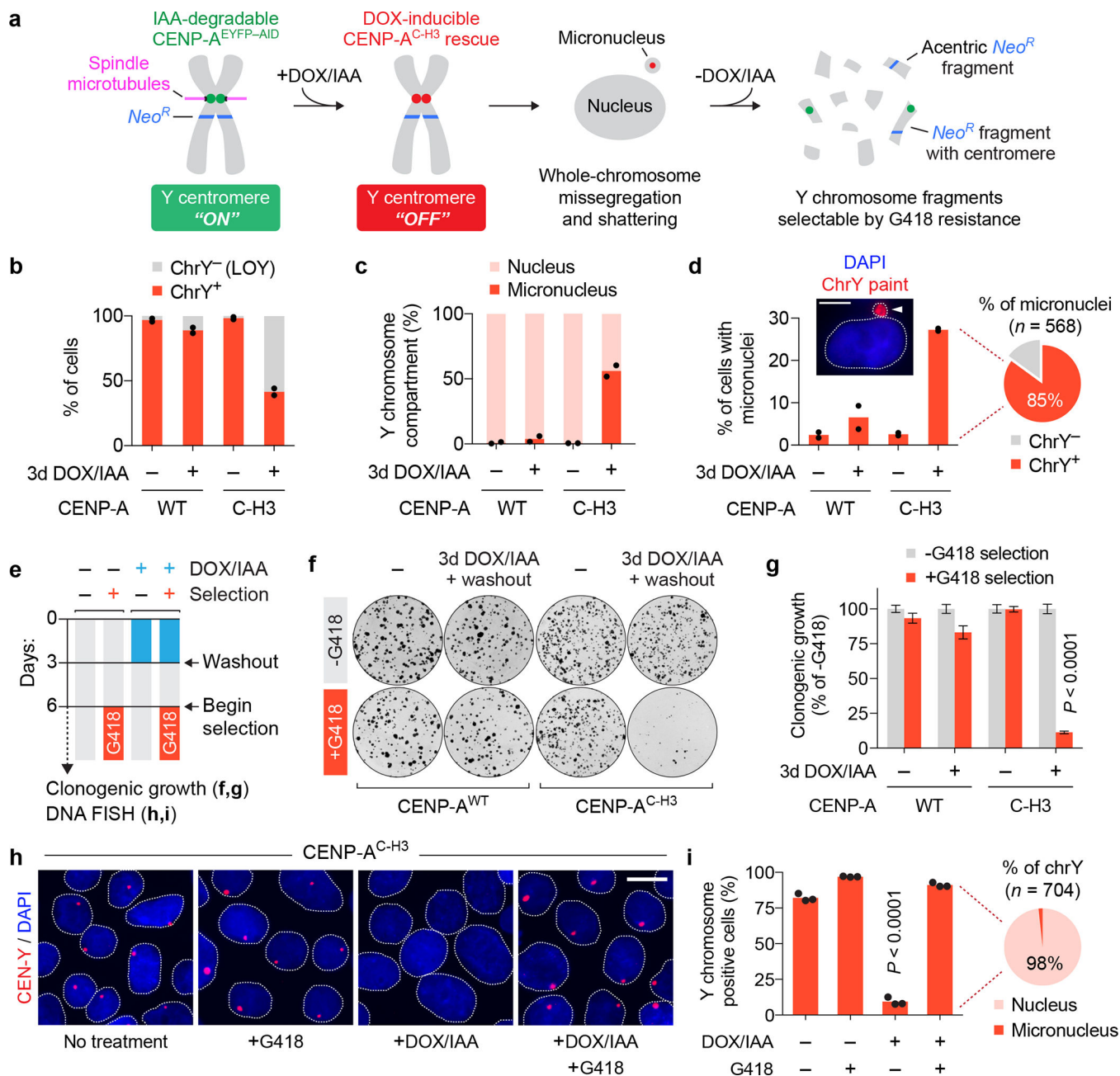
Figure 1 |. A centromere inactivation and chromosome selection system (CEN-SELECT) identifies cells harboring previously missegregated chromosomes.

a) Overview of the CEN-SELECT approach, which combines a CENP-A replacement strategy to induce Y chromosome missegregation and micronucleus-mediated shattering with a CRISPR/Cas9-integrated neomycin-resistance gene (Neo^R). **b-d)** Engineered DLD-1 cells carrying a CENP-A^{WT} or CENP-A$^{C–H3}$ rescue gene were treated with DOX/IAA and quantified by interphase FISH for **b)** Y chromosome loss (LOY), **c)** the compartment of the Y chromosome in chrY-positive cells, and **d)** the proportion of cells with micronuclei. Pie chart shows the fraction of micronuclei carrying a chrY-positive or chrY-negative micronucleus from CENP-A$^{C–H3}$ rescued cells treated with DOX/IAA. Data represent the

mean of $n = 2$ independent experiments from **b,d)** 1,081–2,085 cells or **c)** 861–1,242 Y chromosomes. Scale bar, 5 μm. **e)** Experimental schematic for panels **f-i**. **f)** Representative colony formation plate scans and **g)** quantification. Bar graph represents the mean ± SEM of $n = 9$ biological replicates pooled from 3 independent experiments; P-value derived from two-tailed Student's t-test compared to untreated cells. **h)** Representative interphase FISH images of CENP-A$^{C–H3}$ rescue cells and **i)** quantification. Scale bar, 10 μm. Bar graph represents the mean ± SEM of $n = 3$ independent experiments from 833–918 cells; P-value derived from two-tailed Student's t-test compared to untreated cells. Pie chart represents the fraction of Y chromosomes compartmentalized within the nucleus or micronucleus following DOX/IAA treatment and G418 selection.
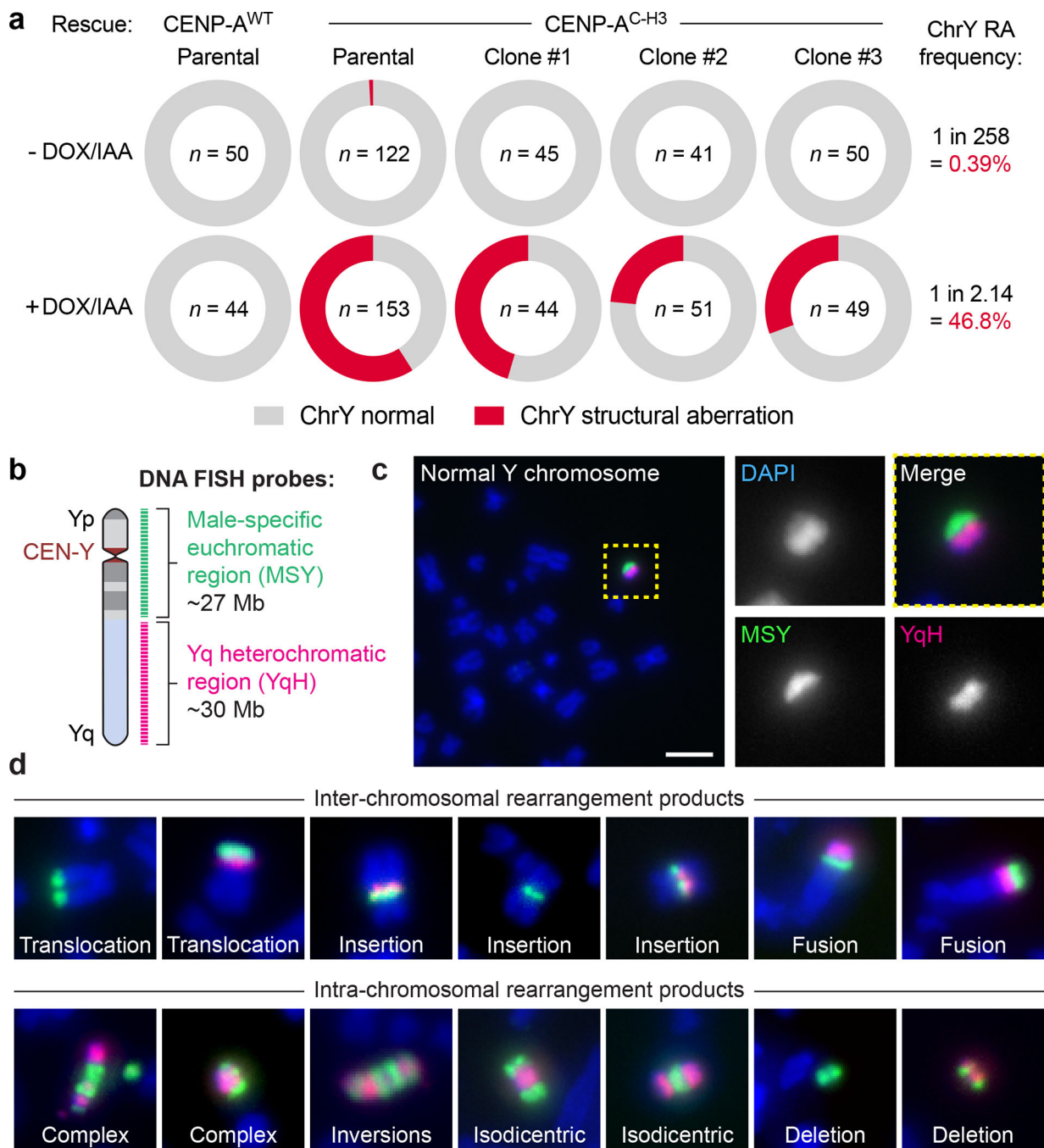
Figure 2 |. Missegregated chromosomes acquire a broad spectrum of structural genomic rearrangement types.

a) Measurements of Y chromosome rearrangement frequencies in parental cells and 3 independent clonal lines following 0d or 3d DOX/IAA treatment and G418 selection. Metaphase spreads were subjected to DNA fluorescence *in situ* hybridization (FISH) using Y chromosome-specific paint probes. n = number of metaphase spreads examined. Parental CENP-A^{C-H3} frequencies were pooled from 3 independent experiments. RA, rearrangement.
b) Schematic of multi-colored DNA FISH probes used to characterize structural anomolies

of the Y chromosome. **c-d)** Representative FISH images of **c)** a normal Y chromosome without visible defects from control metaphases (scale bar, 5 μm) and **d)** examples of derivative Y chromosomes from 3d DOX/IAA-treated, G418-resistant metaphases. See Supplementary Note for a description of each rearrangement type.
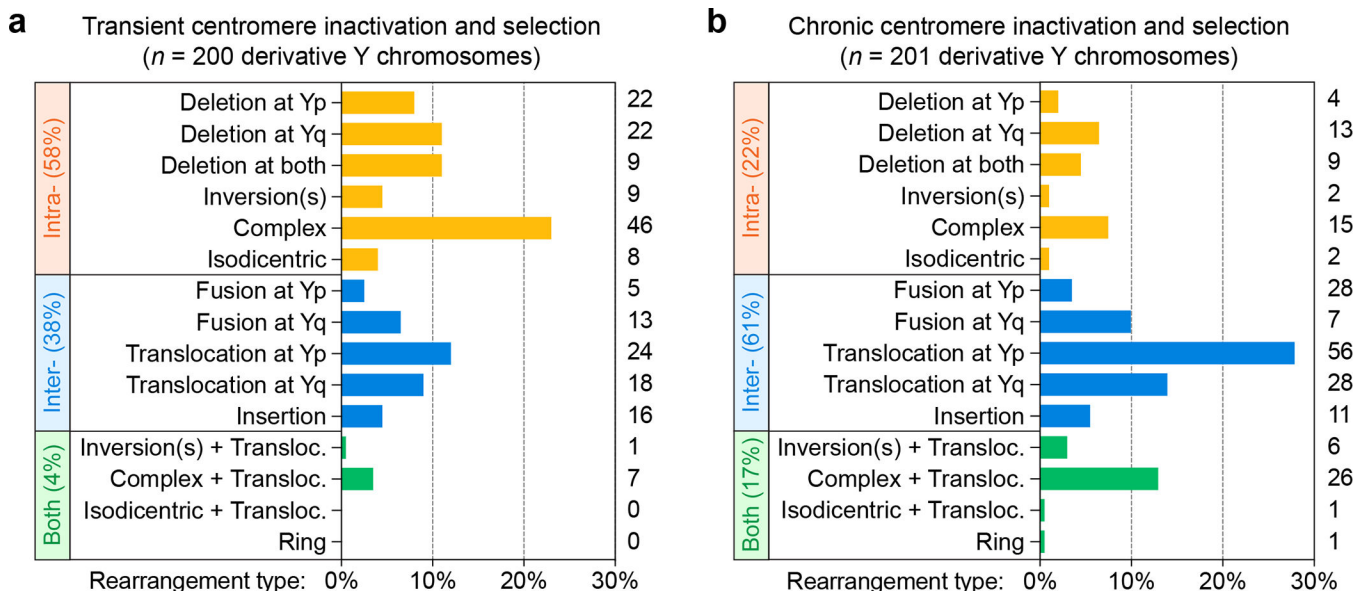
Figure 3 |. Systematic classification of the structural rearrangement landscape.
a-b) The distribution of structural rearrangement types quantified from metaphase spreads using MSY/YqH FISH probes following **a)** transient centromere inactivation induced by 3d DOX/IAA treatment, washout, and G418 selection, or **b)** prolonged centromere inactivation induced by continuous passage in DOX/IAA and G418 (detailed in Supplementary Fig. 6). The number of each case detected is depicted on the right of each graph.
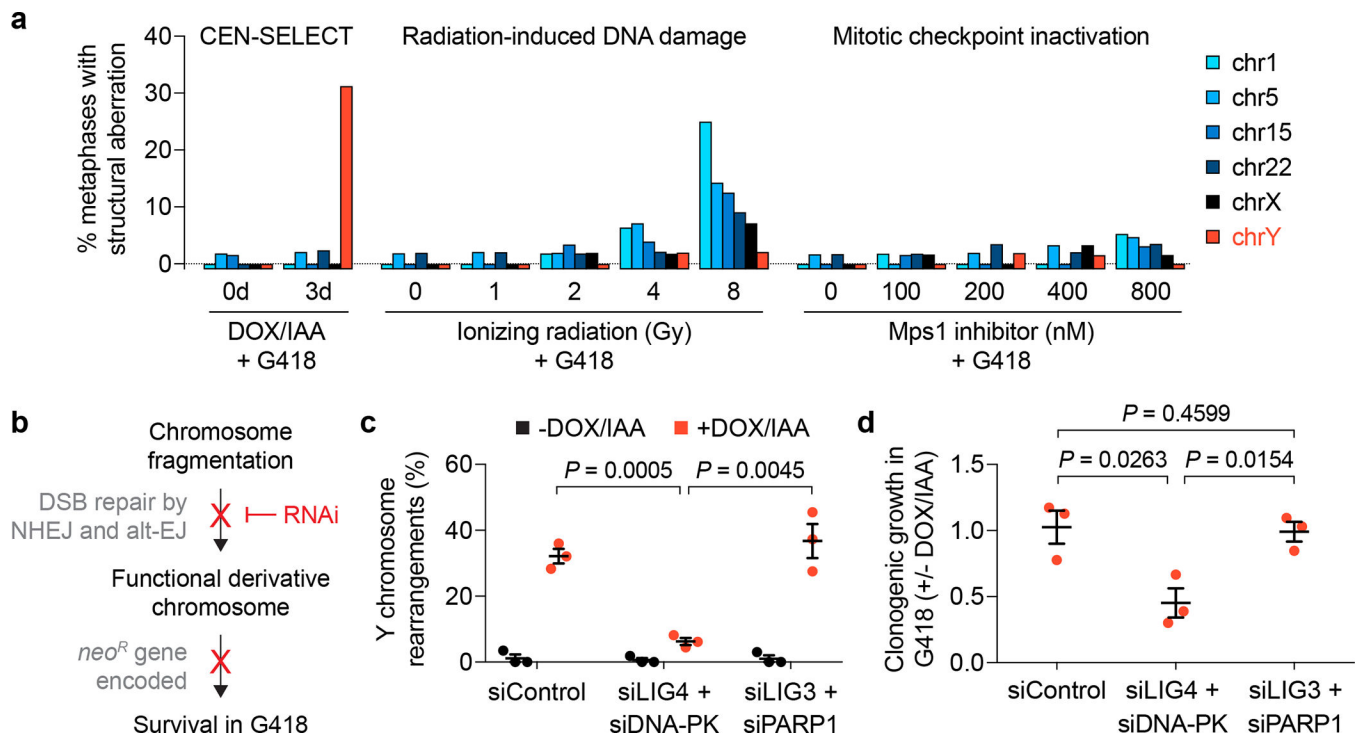
Figure 4 |. Chromosome rearrangements develop with high frequency and specificity through classical non-homologous end joining repair.

a) DLD-1 cells carrying a CENP-A$^{C–H3}$ rescue gene were treated as indicated in Supplementary Fig. 7e, followed by metaphase spread preparation and hybridization to the indicated chromosome paint probes. Metaphases were examined for structural rearrangements affecting each chromosome. Bar graph represents n = 42–65 metaphases scored per chromosome per condition, analysing a total of 1,968 metaphase spreads (exact sample sizes provided in Supplementary Fig. 7g). **b)** Schematic of experimental hypothesis tested in panels **c** and **d**. NHEJ, non-homologous end joining; alt-EJ, alternative end joining. **c-d)** DLD-1 CENP-A$^{C–H3}$ rescue cells were treated with or without 3d DOX/IAA and transfected with the indicated siRNAs simultaneous with DOX/IAA washout for an additional 3d. Cells were then re-plated into G418 medium for **c)** 10d selection followed by metaphase FISH using MSY/YqH probes (102–159 metaphase spreads per condition) or **d)** 14d at single-cell density for colony formation assays. Data in **c** and **d** represent the mean ± SEM of n = 3 independent experiments; P-values were derived from two-tailed Student's t-test comparing groups as indicated.
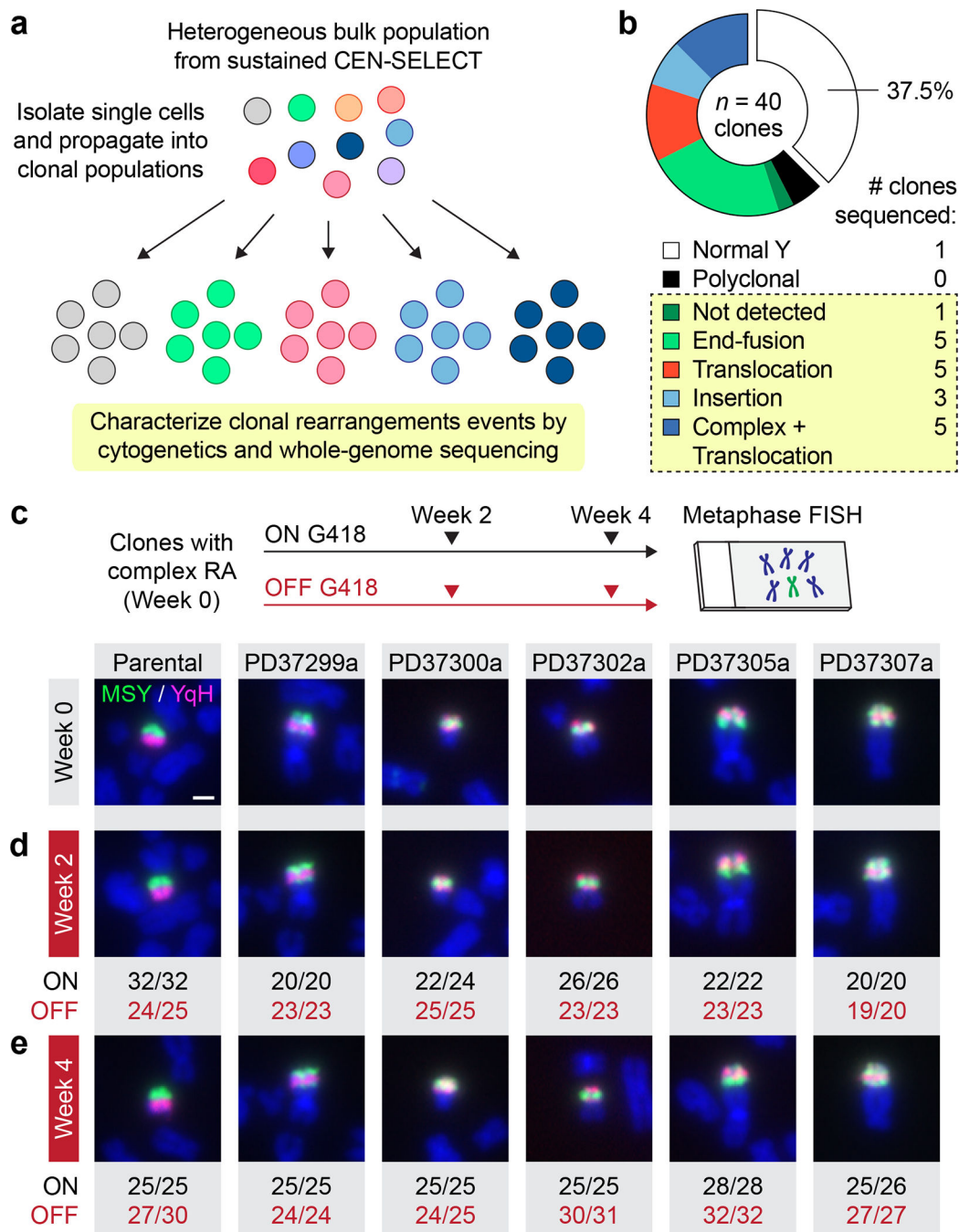
Figure 5 |. Isolation and propagation of single cell-derived clones with genetically stable derivative chromosomes.

a) Schematic of approach used to generate clonally propagated Y chromosome rearrangements from a bulk cell population. **b)** Frequency of Y chromosome rearrangement types obtained from single cell-derived clones. The boxed section indicates clonal rearrangements, and the number of clones subjected to whole-genome sequencing is shown on the right. **c-d)** Experimental schematic and representative metaphase FISH images from the indicated clones, which were passaged in parallel cultures with (ON) or without (OFF)

G418 selection for **c)** 0 weeks, **d)** 2 weeks, and **e)** 4 weeks. Scale bar, 2 μm. Values below the image represent the number of metaphases positive for the depicted derivative chromosome over the total number of metaphases examined. RA, rearrangements.
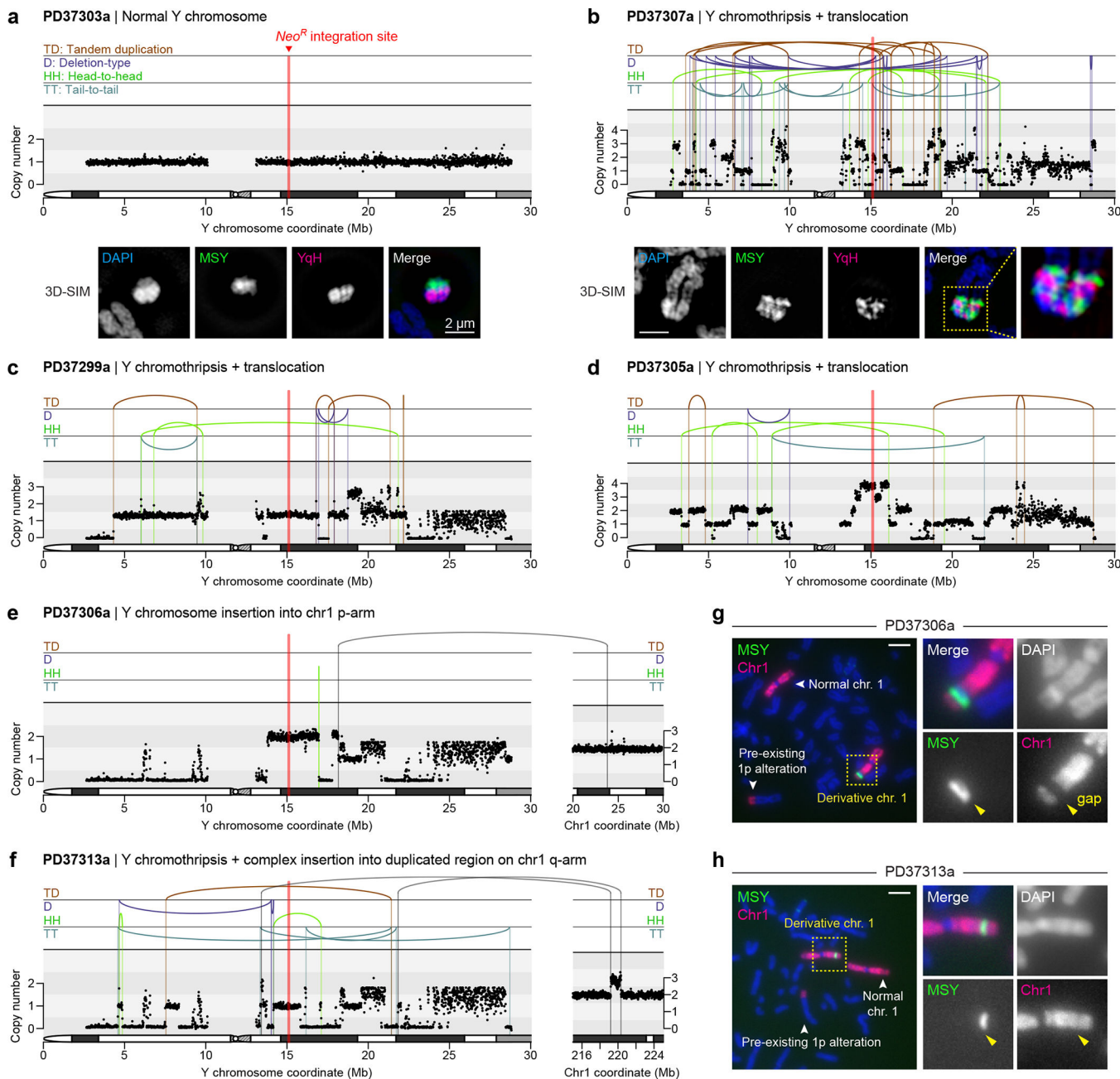
Figure 6 |. Whole-genome sequencing reveals complex rearrangements that include the hallmark signatures of chromothripsis.

a-b) DNA copy-number profiles from WGS (top) and representative metaphase FISH images hybridized to the indicated probes captured by super-resolution microscopy (bottom) from **a)** clone PD37303a with a normal Y chromosome and **b)** clone PD37307a with 83 breakpoints detected across the mappable Y chromosome region. 3D-SIM, 3D structured illumination microscopy. **c-f)** DNA copy-number profiles of additional clones carrying a chromothriptic Y chromosome coupled to **c,d)** translocations, **e)** a simple insertion into chromosome 1p, or **f)** a complex insertion at a duplicated region on chromosome 1q. X-axes of Y chromosome plots are clipped at 30 Mb to exclude the Yq heterochromatic region. **g-h)**

Metaphase FISH images using MSY and chromosome 1 painting probes on clones **g)** PD37306a and **h)** PD37313a. Scale bar, 5 μm.
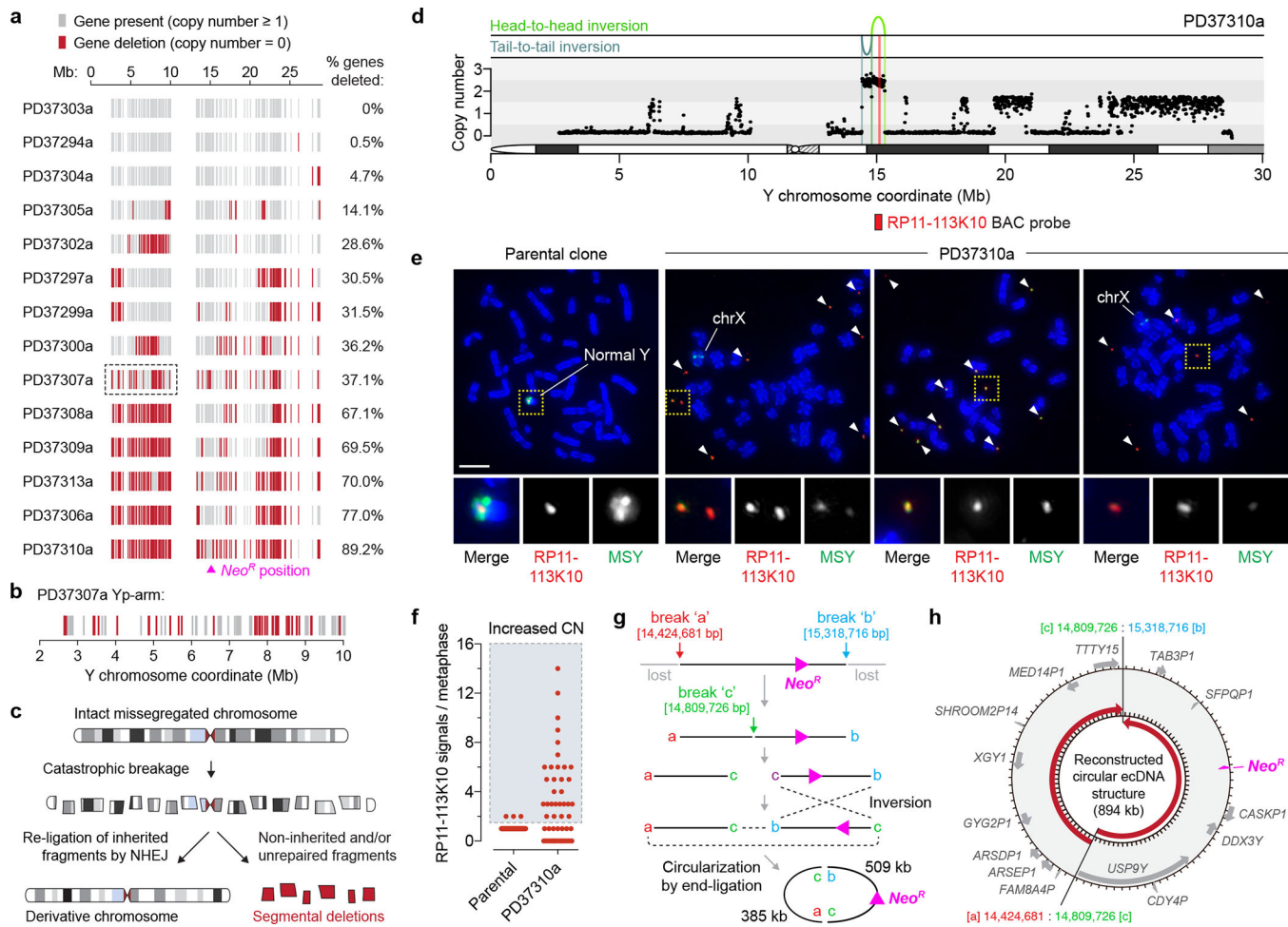
Figure 7 |. Gene disruption and extrachromosomal DNA amplification from chromosome missegregation-induced rearrangements.

a) Each grey vertical line represents an individual gene or pseudogene depicted at its chromosomal start position, and red lines represent a copy-number of zero. Clones are ranked from fewest to most gene deletions. **b)** Magnification of clone PD37307a (boxed region in **a**) exhibiting oscillating patterns of gene retention and deletion within an 8 Mb segment. **c)** Schematic of chromosome shattering and reassembly events resulting in a derivative chromosome harboring rearrangements with interspersed deletions. **d)** DNA copy-number profile of clone PD37310a showing extensive Y chromosome loss except for the region harboring the selection marker accompanied by two inversions. **e)** Images of metaphase spreads prepared from the parental or PD37310a clone and hybridized to MSY (green) and RP11–113K10 BAC (red) probes recognizing the region shown in **d**. Arrows denote extrachromosomal DNA fragments hybridizing to the RP11–113K10 probe, and regions of the X chromosome partially hybridize to MSY probes due to X-Y sequence homology. Scale bar, 5 μm. **f)** Quantification of **e**. Each data point represents an individual metaphase spread derived from the parental clone ($n = 48$) or PD37310a clone ($n = 56$). CN, copy-number. **g)** Schematic depicting the predicted steps leading to the generation of the extrachromosomal DNA (ecDNA) element through the circular reassembly of two broken

DNA fragments. **h)** Reconstructed ecDNA sequence from WGS. Genes and pseudogenes in the corresponding region are shown, and red arrows depict 5' to 3' orientation.